Journal of
Synchrotron Radiation

ISSN 0909-0495

Received 26 September 2012
Accepted 29 November 2012

Using an in-vacuum CCD detector for simultaneous small- and wide-angle scattering at beamline X9

Lin Yang

Photon Sciences Directorate, Brookhaven National Laboratory Upton, New York, USA.
E-mail: lyang@bnl.gov

The implementation of simultaneous small- and wide-angle X-ray scattering at beamline X9 of the National Synchrotron Light Source is described. By utilizing an in-vacuum CCD detector with a truncated cone-shaped head and positioned at $\sim 20^\circ$ off-axis from the direct beam, the overlap of the scattering angle coverage between the wide-angle detector and the conventional small-angle detector is maximized. The combined q-range for measurements in transmission geometry is typically 0.006–2.0 Å^{-1} at 13.5 keV, with overlapping data within the range $\sim$0.1–0.2 Å^{-1}. Simultaneous data collection can also be performed in grazing-incident measurements of flat substrate-supported samples, in which case the wide-angle detector can collect the scattering data along the sample normal as well as parallel to the sample surface without blocking the direct beam. Data processing and correction procedures will be discussed and examples presented.

Keywords: simultaneous; SAXS; WAXS; GISAXS; GID.

1. Introduction

Simplistically speaking, X-ray scattering at scattering vector $q = (4\pi/\lambda)\sin\theta$ corresponds to the characteristic length scale of $d \simeq 2\pi/q$. Here, λ is the X-ray wavelength and 2θ is the scattering angle. When the sample contains structures on multiple length scales, data at both small scattering angles (SAXS) and wide scattering angles (WAXS) need to be collected. For example, in measurements of proteins in solution, the SAXS data correspond to the overall shape of the proteins while the WAXS data reveal details of their internal structure. Similarly, in grazing-incidence measurements of self-assembled thin films of small organic molecules such as lipids, the SAXS data contain information on the supramolecular structure (*e.g.* layers) while the molecular packing within the layers produces diffraction peaks in the WAXS data.

Usually, SAXS and WAXS data are obtained in separate measurements of long and short sample-to-detector distances. Doing so requires the scattering instrument to be reconfigured and therefore can be time-consuming. Separate SAXS and WAXS measurements are also not ideal if the structure within the sample depends on environmental conditions that cannot be easily reproduced, for instance when the structure in the sample changes very quickly within the time scale of data collection or is history-dependent.

At beamline X9 at the National Synchrotron Light Source (NSLS) of Brookhaven National Laboratory (BNL), we recently constructed an instrument that can simultaneously collect SAXS and WAXS data. The basic optical layout of the beamline has been described elsewhere (Allaire & Yang, 2011). Here, we focus on the implementation of simultaneous SAXS/WAXS data collection and the associated data-processing procedures. The central component in this implementation is a vacuum-compatible CCD detector that is integrated into the scattering beam path. This detector has a truncated cone-shaped head and is positioned off-axis from the direct beam. Therefore there is minimal obstruction of scattering data by the detector housing. On the other hand, this unusual geometry of the detector does complicate the conversion of the scattering pattern into reciprocal-space coordinates. In this paper the design of the WAXS detector is first described, followed by a brief description of data processing and correction procedures, and finally examples of how the detectors are utilized in various measurements at beamline X9. Technical details involved in data processing and correction are given in Appendices *A*, *B* and *C*.

2. X9 WAXS detector

Simultaneous collection of SAXS and WAXS data has been previously reported at a number of synchrotron beamlines. This is often achieved by mounting a linear detector (Bras *et al.*, 2003; Jeng *et al.*, 2009) or small area detector (Urban *et al.*, 2003; Rueda *et al.*, 2006) alongside the scattering beam path near the sample position. More elaborated schemes of SAXS/WAXS data collection involve specially designed WAXS detectors, with an aperture in the detector front surface for the scattered X-rays at small angles to pass through (Pokric *et al.*, 2002; Weigand *et al.*, 2009). At the time when beamline X9 was

designed and constructed (*ca* 2006–2008), these detectors were generally not commercially available, perhaps limited by their costs, complexity and lack of flexibility in their uses in experiments. It should be pointed out, however, that at least a couple of SAXS/WAXS systems are now being marketed by Rayonix and Rigaku. It is also worth noting that the recent serial crystallography experiments at the Linac Coherent Light Source utilized multiple detectors in a SAXS/WAXS configuration (Chapman *et al.*, 2011).

The design of the X9 WAXS detector is schematically shown in Fig. 1(*a*). It resembles one-quarter of the WAXS detector described by Pokric *et al.* (2002) in that the detector is positioned off-axis from the direct beam, therefore the bulk of the detector body can be moved out of the path of the scattered X-rays. It is designed to be vacuum-compatible so that it can be integrated into the scattering beam path for SAXS. Moreover, the detector housing has the shape of a truncated cone, further reducing the obstruction of scattered X-rays by the detector body. The overlap between the scattering angles covered by the SAXS and WAXS detectors is therefore maximized. Unlike the Pokric detector, the X9 detector utilizes one single fiber-optic taper and it does not need to be reshaped. The fabrication of the detector was therefore fairly routine.

This design was realised by Photonic Science Ltd (East Sussex, UK) using a Kodak 4301E CCD sensor (2084 × 2084 pixels, 24 µm pixel size). The body of the detector is 160 mm in diameter and reduced to ∼140 mm in diameter at the front surface. The Gadox(Tb) phosphor that converts X-rays into visible photons is directly deposited (15 mg cm^{-2}) onto the fiber-optic taper, which is 135 mm in diameter. The phosphor is shielded from ambient light by a 100 µm-thick Sigradur (vitreous carbon) window. The demagnification of the fiber-optic coupling between the phosphor and the CCD sensor is 2.12, resulting in almost 20% of light transmission (Gruner *et al.*, 2002). This is reasonably high for CCD detectors and gives the detector good sensitivity.

When projected onto the phosphor, the outline of the CCD sensor is a 106 mm square, or ∼150 mm diagonally, and extends beyond the circumference of the phosphor. Thus the direct beam can pass through unobstructed even when its position is nominally within the boundary of the CCD images collected by the WAXS detector (Fig. 1*b*). This is particularly useful in grazing-incident diffraction (GID) measurements, in which the information near the q_r and q_z axes can be captured without the need of a beamstop in front of the WAXS detector (q_r and q_z are the components of the scattering vector parallel and perpendicular to the flat sample, respectively; see the example below in §4.3).

The detector is housed in a large vacuum chamber (Fig. 1*c*) and mounted on motorized translation stages so that its relative position to the direct beam can be adjusted. The detector mount can also be manually rotated about the axis of the direct beam to capture different quadrants of the azimuthal angles. Experiments can be conducted without any barrier between the sample and the detector, either in rough vacuum or at atmospheric pressure, for instance when the chamber is filled with helium gas. Alternatively, the sample can be located in air, separated by a vacuum window from the WAXS detector under vacuum. In this case, collecting unobstructed WAXS data is still possible, either using a large vacuum window or by positioning the sample sufficiently close to a thin and small vacuum window when the scattering background from the window must be minimized.

The Sigradur window provides good X-ray transmission (93% at 8 keV). However, it is quite brittle and not suitable in an environment that sees heavy user activities. We have recently adopted a black Kapton window after the Sigradur window was damaged. The black Kapton film (1 mil thick, purchased from McMaster-Carr, Atlanta, GA, USA) is stiffened using an office laminating sheet so that it can be

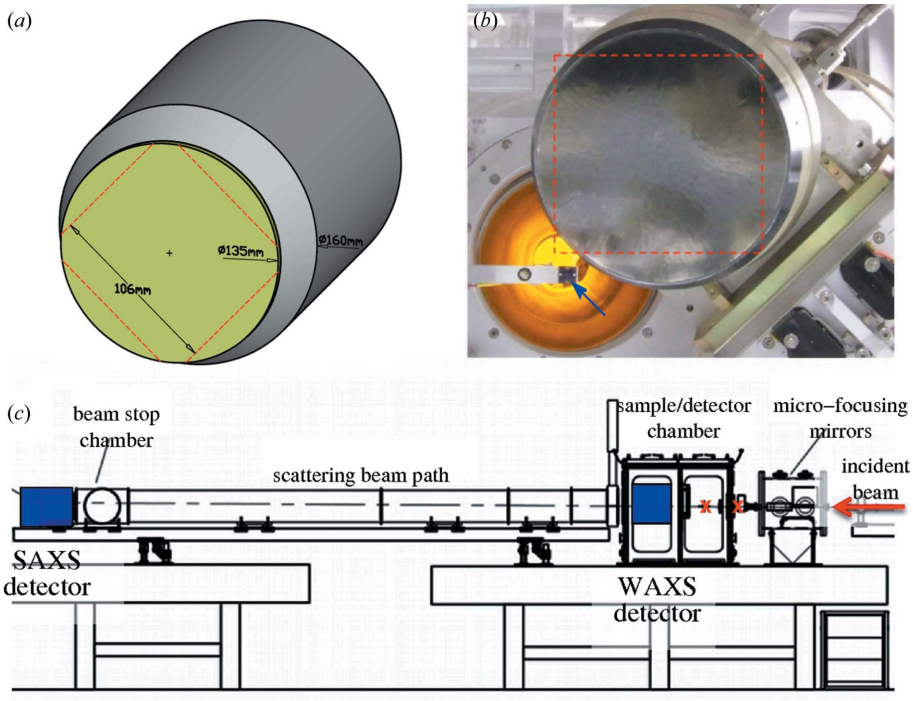

Figure 1
(*a*) Schematic design of the X9 WAXS detector. (*b*) The actual detector mounted in the detector chamber at X9, viewed from near the sample position. The red dashed lines denote the outline of the CCD sensor when projected onto the detector surface. The orange color is due to the Kapton window at the end of the SAXS flight tube. The arrow points to the photodiode used for sample alignment in grazing-incidence measurements. (*c*) Layout of the X9 endstation, showing the location of the SAXS and WAXS detectors, as well as the possible locations for the sample, as marked by the red X marks. The X-ray beam enters the endstation from the right. The optical layout of the beamline has been previously described (Allaire & Yang, 2010).

easily mounted on the window frame. At X-ray energies above 12 keV, at which the beamline is most often operated, the laminated window still provides X-ray transmission over 98%. Any non-uniformity in X-ray transmission by the window due to thickness variation can be corrected by the flat-field correction.

The WAXS detector is controlled using macros defined under the beamline control software *SPEC* (http://www.certif.com/). These macros direct data collection, archive the resulted images onto the local computer, and extract region-of-interest information from these images (see §4.1). Their communication with the detector is accomplished *via* a simple software device server (written using Windows DLLs provided by Photonic Science) that relays commands to the detector controller over the beamline computer network. These same macros also control the SAXS detector (either a Mar165 or a Pilatus 300K) following a similar protocol.

3. Data processing and correction

The scattering intensity must be represented as a function of the scattering vector for the purpose of data interpretation. It is therefore necessary to translate the pixel positions in the scattering patterns into the corresponding scattering vector. Sometimes it is also necessary to translate a given scattering vector back to the pixel position, for instance, for the purpose of comparing theoretical prediction directly with the scattering pattern.

Unlike in the conventional geometry for scattering measurements, our WAXS detector is not positioned perpendicular to the direct beam. This unusual orientation adds some complexity to the geometric conversion. While the mathematics involved in this conversion is relatively straightforward, it is described in Appendix *A* for readers that may find it useful when using a similar scattering geometry. The procedure for calibrating the detector orientation using standard samples is also given in Appendix *B*.

Before data interpretation, the scattering intensity also needs to be corrected to account for device-dependent and scattering-geometry-dependent factors. The corrections common to CCD detectors are well established (Gruner *et al.*, 2002; Barna *et al.*, 1999).

The flat-field and image-distortion corrections are intrinsic to the construction of the detector and can be applied to the scattering patterns regardless of the geometry of the scattering measurements. At X9, the image-distortion correction is handled by the software provided by the manufacturer, and we utilize X-ray fluorescence from a solution sample as the uniform radiation source for flat-field correction (see §4.1).

On the other hand, the polarization correction and the pixel solid angle correction are determined by the scattering geometry. The solid angle correction arises from differences in the solid angle within which each pixel collects scattered X-rays. It contains contributions from the distance between the pixel and the sample as well as the apparent reduction in pixel size owing to non-normal incidence of X-rays onto the detector (Barna *et al.*, 1999). The polarization and solid angle correction factors, expressed as functions of the detector geometric parameters, are given in Appendix *C*.

Depending on the sample and the type of scattering measurements, other corrections (*e.g.* Lorentz correction and absorption correction) may be necessary. These experiment-specific corrections will not be discussed here.

4. Applications of the X9 SAXS/WAXS detector system

4.1. As fluorescence detectors

We have utilized both SAXS and WAXS detectors as fluorescence detectors, most often in solution scattering measurements, for flat-field correction, sample alignment and X-ray energy calibration. In solution scattering measurements at X9, the sample is located in a 1 mm glass capillary sealed by O-rings across the evacuated beam path (Yang, 2005) and mounted on the front side of the sample/detector chamber (Fig. 1*c*). During sample alignment, the X-ray beam is steered by the primary focusing mirrors to point to the center of the capillary tube. While sample alignment is more commonly and accurately performed by moving the sample instead of the beam, doing so would require a bellow downstream of the sample, limiting the range of scattering angles in the WAXS pattern. On the other hand, the smallest step size of the steering mirror translates to a beam displacements of $\sim$37 µm at the sample and $\sim$49 µm on the SAXS detector, which are small compared with the capillary diameter of 1 mm and the pixel size of 172 µm on the Pilatus SAXS detector. Furthermore, the actual beam position on the detector can be read directly from the SAXS pattern since the beamstop is semi-transparent to the direct beam.

The fluorescence emission from a solution sample is isotropic and therefore an excellent source for flat-field illumination. However, in the image of this emission recorded by the detector [Figs. 2(*a*) and 2(*b*)], the intensity is influenced by (i) the geometric correction factor $F_{\rm s.a.}$, discussed in Appendix *B* [this is the primary factor that contributes to the intensity variation across the image in Fig. 2(*b*)], as well as (ii) absorption by the solution sample, which may depend on both θ and φ given the cylindrical shape of the capillary tube and therefore difficult to quantify. Fortunately, these correction factors are identical to those needed to correct for X-ray scattering intensity measured in the same sample cell (neglecting the difference in sample absorption owing to the different energies between the incident and the emitted X-rays). Therefore, using the fluorescence image from a solution sample as the reference for flat-field correction can in fact simultaneously account for all required corrections except for the polarization correction, which can be calculated easily using equation (19).

It should be pointed out that these fluorescence images also contain the scattering contribution from unabsorbed X-rays. At X9, the X-ray energy used for solution scattering measurements is usually 13.5 keV, just above the *K* absorption edge of bromine. X-ray transmission through a 1 mm capillary filled with the 5 *M* NaBr solution that we typically use for

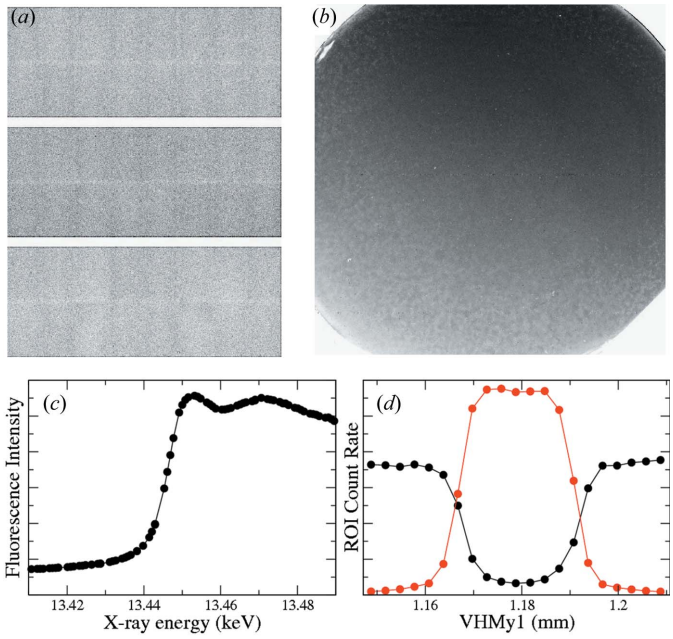

Figure 2
Flat-field images recorded on (*a*) the Pilatus 300k SAXS detector and (*b*) the WAXS detector, using the fluorescence from a 5 *M* NaBr solution in the solution scattering sample cell as the source. The gray scale in the images is set so that the darkest to the brightest gray levels represent 100% to 70% of the maximum intensity. (*c*) Energy scan across the Br *K*-edge. The region of interest (ROI) is a square of 200 × 200 pixels near the center of the WAXS detector. (*d*) ROI counts on the WAXS detector (red symbols, fluorescence intensity, unattenuated incident beam) and on the SAXS detector (black symbols, transmitted intensity of the direct beam, with $\sim 10^{-4}$ attenuation), during the scan of the elevation of one end of the vertical focusing mirror, which is 0.43 m long, to steer the beam across the capillary, which is located at 7.9 m downstream of the mirror. The ROI on the SAXS detector captured the direct beam during the full range of the scan and the beamstop upstream of the detector was removed.

calibration is 9% [see Fig. 2(*d*) and descriptions below]. Based on the scattering intensity of water, the scattering contribution to the total recorded intensity is estimated to be ∼6% near the water scattering peak in the WAXS pattern (upper right corner) and <1% away from it and therefore can be neglected. Alternatively, the scattering contribution can be subtracted based on the scattering intensity from a similar sample that does not produce fluorescence (*e.g.* a NaCl solution).

For energy calibration, the WAXS detector is used as a point detector. A region of interest (ROI) is defined as a macro counter under *SPEC*, which extracts the total counts within the ROI using external Python scripts. The resulting energy scan is shown in Fig. 2(*c*). Note that the fluorescence intensity is distorted toward the ends of the energy range. Specifically, the intensity decreased because the X-ray beam position swept across the capillary during the scan (confirmed by the beam-position monitor upstream of the sample). However, this is acceptable for the purpose of X-ray energy calibration since the distortion does not affect the location of the absorption edge.

The same WAXS ROI can also be used for sample alignment [red symbols in Fig. 2(*d*)]. When the X-ray beam is steered across the capillary tube that contains the fluorescence emitter, the center of the fluorescence intensity peak in the scan gives the ideal X-ray beam position. Conversely, an ROI can be defined on the SAXS detector to measure the transmitted beam intensity, using attenuated beam without the beamstop. The ideal beam position is now given by the center of the valley [black symbols in Fig. 2(*d*)] that corresponds to X-ray absorption by the sample. The results of the two methods are consistent with each other.

The SAXS detector can be similarly used for sample alignment in grazing-incident scattering measurements to precisely locate the reflection from the sample to the point on the detector that corresponds to the required incident angle. In this case the expected position of specular reflection is defined as the ROI. At the typical camera length of 2.5 m, the pixel size of 0.16 mm (Mar165 in 1024 × 1024 mode) corresponds to an incident angle precision of ∼0.004°. The actual accuracy of the calculated incident angle is better than that since the peak position can be determined to a precision better than the width of a pixel.

4.2. Protein solution scattering

X-ray scattering has been increasingly frequently utilized to characterize the structure of proteins in solution under near native conditions. While the most basic information comes from low-q data (up to ~ 0.3 Å^{-1}), new developments in data analysis now require data at higher q as well. For instance, the program *GASBOR* for molecular envelope modeling makes use of scattering data up to ~ 0.8 Å^{-1} (Svergun *et al.*, 2001). And the possibilities of exploiting data at even higher q values (up to ~ 3 Å^{-1}) to detect small structural changes and characterize protein fold are also being explored (Makowski, 2010).

Solution scattering measurements are relatively short (<1 min of exposure time per scattering pattern). Simultaneous SAXS/WAXS data collection without having to spend additional time and effort on modifying the beamline configuration results in efficient utilization of the available beam time. The solution scattering instrumentation at X9 has been previously reported (Allaire & Yang, 2010). We have since updated the procedure for data processing to fully take advantage of the WAXS detector, as described below.

Each set of simultaneously collected SAXS and WAXS images are first converted into one-dimensional scattering profiles. During this process, dark-current subtraction and other necessary corrections are performed on each individual image. The SAXS and WAXS profiles are then merged by scaling the WAXS data to match the SAXS and WAXS intensity within the overlapping q-range. Before buffer subtraction, multiple merged scattering profiles collected from the same sample are averaged together, excluding outliers due to either air bubbles trapped in the sample during exposure (flowing sample) or radiation damage (stationary sample).

The quality of solution scattering data critically depends on precise buffer scattering subtraction, which requires knowledge of the transmitted beam intensity, with contributions from both the incident beam intensity and the sample

absorption, as well as the volume fraction of proteins in the solution (Makowski, 2010). While X-ray scattering beamlines are usually equipped with monitors that measure the transmitted beam intensity, in general the protein volume fraction is difficult to quantify and often estimated based on the protein concentration and an assumed protein density. With simultaneous SAXS/WAXS, the water scattering peak at $\sim$2.0 Å^{-1} is usually present in the WAXS data. The amplitude of this peak, A_w, depends directly on several factors: (i) the volume of the solvent in the sample (excluding proteins) illuminated by X-rays, the scattering from which needs to be subtracted, (ii) the incident beam intensity, and (iii) the absorption of X-rays by the sample. Scaling the data based on A_w therefore accounts for all these factors that can affect the accuracy of buffer subtraction, without having to resort to the ill-defined protein volume fraction. We have found this method very reliable for data collected at X9 (Fig. 3) and our users now routinely use it.

Solution scattering measurements are often performed using a fixed sample cell to ensure reproducible empty cell scattering and volume of the sample that contributes to scattering. Buffer subtraction based on water scattering intensity relaxes the requirement of constant sample volume, and therefore opens up new possibilities to speed up data collection. For instance, a windowless sample changer in which solution samples are suspended over open apertures is being pursued at X9. The samples can be loaded into the sample changer and measured sequentially, while another changer is being prepared. Decoupling filling the samples from measuring them minimizes dead-time between measurements.

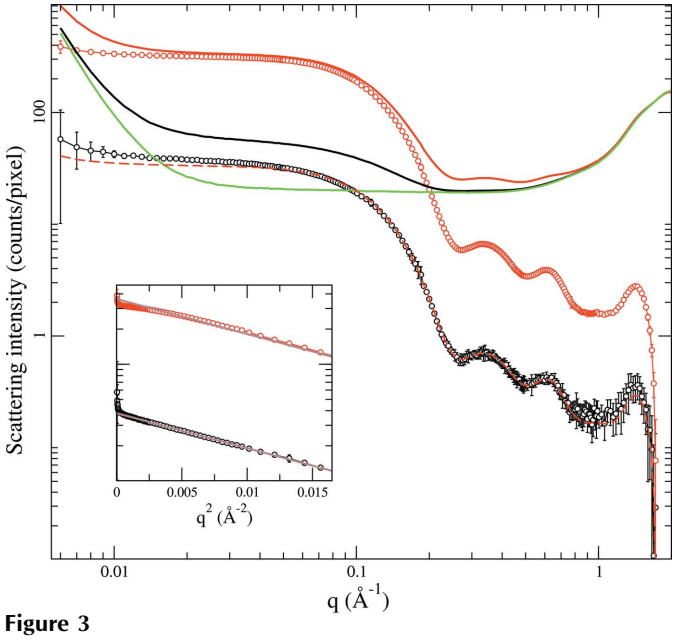

Figure 3
Merged SAXS/WAXS data collected at X9 (courtesy of Marc Allaire) from lysozyme solutions at nominal concentrations of 5 mg ml^{-1} (black) and 50 mg ml^{-1} (red). Solid lines and symbols represent data after scaling and after subtraction of buffer scattering (green), respectively. The corresponding volume fractions of lysozyme are 0.37% and 3.70%, based on the assumed protein density of 1.35 mg ml^{-1}. Scaling was performed by simply matching sample and buffer scattering intensity near q = 2.0 Å^{-1}. As a result, the background-subtracted intensity artificially approaches 0 at the same q. The curves are essentially parallel to each other on a log scale, indicating that the background-subtracted data are proportional to the sample concentration and therefore good background subtraction (the red dashed line is scaled down from the 50 mg ml^{-1} data by a factor of 9.5). The low-q data for the 50 mg ml^{-1} sample is apparently affected by the inter-particle structure factor, as shown in the Guinier plot in the inset.

4.3. Grazing-incidence studies

A significant portion of the users at X9 are also users that perform nanofabrication on organic materials at BNL's Center of Functional Nanomaterials (CFN). The two-detector configuration at X9 is well suited for studying these nanofabricated samples. While the grazing-incident WAXS (GIWAXS, also known as GID) data provide information on the internal structure of these materials (*e.g.* packing of polymer chains and their orientations), the grazing-incident SAXS data reveal the nature of the supramolecular structures resulting from the nanofabrication process. Examples of these experiments are beginning to emerge in the literature (Hlaing *et al.*, 2011; Kim *et al.*, 2011). The GISAXS and GIWAXS patterns are usually collected sequentially, owing to the difference in the respectively required exposure times, as well as to avoid the shadow of the WAXS detector in the GISAXS pattern. Switching between the GISAXS and GIWAXS measurements is accomplished by simply moving the WAXS detector by a few millimeters and takes minimal time.

GIWAXS patterns generally appear warped, mainly owing to the curvature of the Ewald sphere, which is most severe near the direction of sample normal (Yang & Yang, 2009), as seen in Fig. 4(*b*). The distortion is further complicated by the WAXS detector geometry. Unwarping the image can be accomplished by utilizing the data conversion worked out in Appendix *A* and has been implemented in the software developed at the beamline, as shown in Fig. 4(*c*). Clearly, extraction of orientation information (*e.g.* orientation distribution of polymer chains) should be performed only on unwarped intensity maps.

5. Summary

The in-vaccum WAXS detector at beamline X9 allows for simultaneous SAXS/WAXS data collection for most experiments and fast switching between SAXS and WAXS configurations in others. Its use has resulted in reduced burden on beamline operations for configuration changes and more efficient use of beam time. We have explored creative use of this detector, as a fluorescence detector and for buffer scattering subtraction in solution scattering measurements. Similar designs utilizing vacuum-compatible area detectors for WAXS are being adopted by the LiX beamline at the new NSLS-II storage ring. The conversion and correction calculations worked out for the X9 detectors are generally applicable to scattering measurements utilizing area detectors. They have been implemented in the *view.gtk* and *pyXS* programs, which are documented and available for download at the website of beamline X9, http://www.bnl.gov/ps/x9/software/.

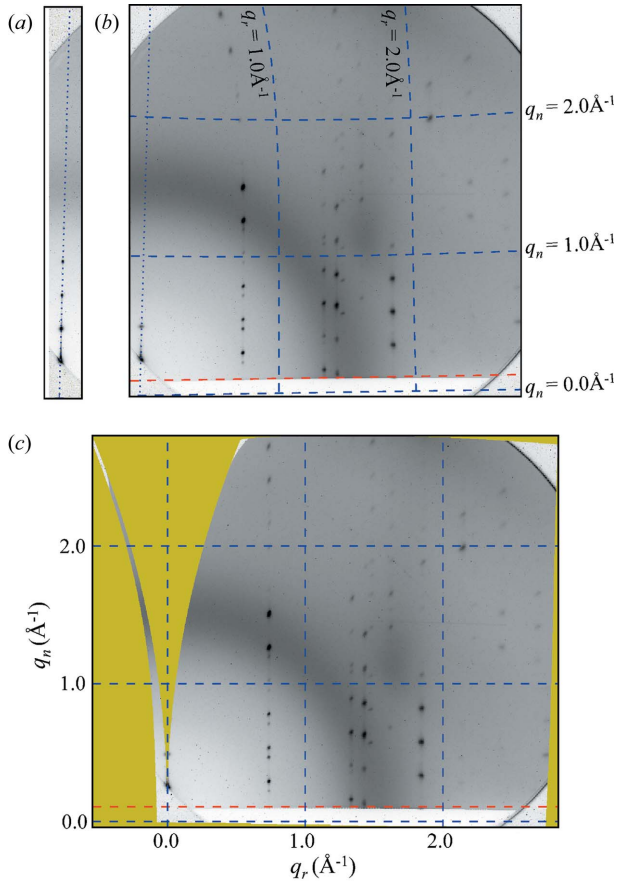

Figure 4
Example of GID data collected at X9 (courtesy of Hoichang Yang of Inha University) (*a*) while the sample is being rotated to vary the incident angle and (*b*) at a fixed incident angle (0.6°). The blue dotted lines indicate the direction of the sample normal, which is also the trace of specular reflection from the sample in (*a*), on which the (00*L*) diffraction peaks are located. The blue dashed lines that denote constant q_r and q_z positions of 0, 1.0 and 2.0 Å^{-1} are distorted owing to the curvature of the Ewald sphere. These apparent distortions disappear in (*c*), where the data shown in (*b*) have been translated into a $q_r - q_z$ map using the conversions described in the text. The areas colored yellow are not accessible in the measurement. The red dashed lines in (*b*) and (*c*) indicate the expected Yoneda peak position. Note that the size of the diffraction peaks becomes progressively larger at higher q because of the finite beam size on the sample in the grazing-incident geometry. The sample-to-detector distance is ∼27 cm.

APPENDIX *A*
Conversion between a pixel position and the corresponding *q*-vector

In the most general case the orientation of the WAXS detector can be described by three parameters. As illustrated in Fig. 5, the orientation of the X9 WAXS detector can be defined by the following: (i) the off-axis angle of the detector, τ; (ii) the orientation of the rotation axis of this tilt, $\hat{\tau}$, denoted as ψ and defined to be 0 if it is along the columns of pixels and pointing up (y-axis); and (iii) for grazing-incident measurements the amount of additional detector roll, χ, about the beam axis after the off-axis tilt. For the configuration shown in Fig. 1(*b*) (the sample normal is along the y-axis), $\tau \simeq -17°$, $\psi = 45°$ and $\chi = 0$.

The conversion from a pixel position (x_0, y_0) to the corresponding scattering vector can be performed as the following. Define the location where the incident X-rays along the $-z$-axis hits the detector as the zero pixel position ($x_0 = y_0 = 0$), and the sample position at distance d upstream as the origin of the laboratory coordinate system ($x = y = z = 0$) (Fig. 5). The physical position of the pixel $\mathbf{r} = (x, y, z)$ is then given by consecutive rotations of the coordinate system about the z-axis by ψ, then about y-axis by τ, and finally about the z-axis by $\chi - \psi$,

$$\begin{pmatrix} x \\ y \\ z \end{pmatrix} = \mathbf{R}\begin{pmatrix} x_0 \\ y_0 \\ 0 \end{pmatrix} - \begin{pmatrix} 0 \\ 0 \\ d \end{pmatrix}, \tag{1}$$

with the overall rotation matrix

$$\begin{aligned} \mathbf{R} &= \mathbf{R}(\chi, z)\mathbf{R}(-\psi, z)\mathbf{R}(\tau, y)\mathbf{R}(\psi, z) \\ &= \begin{pmatrix} R_{11} & R_{12} & R_{13} \\ R_{21} & R_{22} & R_{23} \\ R_{31} & R_{32} & R_{33} \end{pmatrix} \end{aligned} \tag{2}$$

given by the individual matrices $R(\alpha, a)$ that correspond to counter-clockwise rotations about the a-axis by angle α,

$$\mathbf{R}(\alpha, z) = \begin{pmatrix} \cos\alpha & -\sin\alpha & 0 \\ \sin\alpha & \cos\alpha & 0 \\ 0 & 0 & 1 \end{pmatrix}, \tag{3}$$

where α should be substituted with χ, $-\psi$ and ψ, and

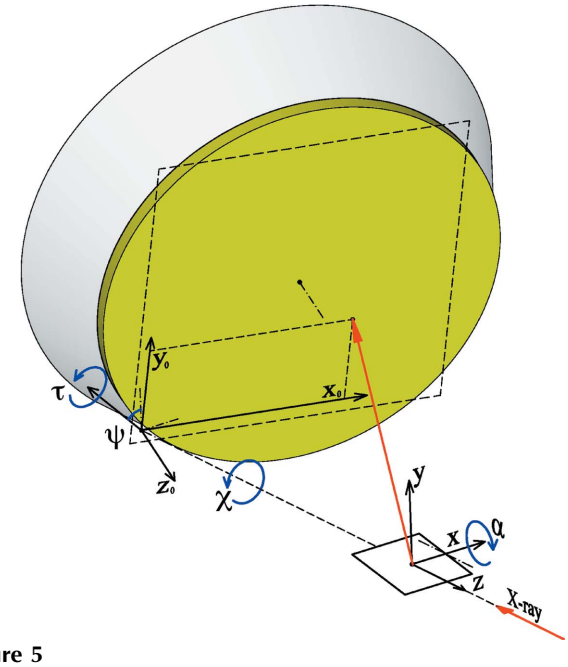

Figure 5
Illustration of the typical positioning of the WAXS detector at X9 and the angles that define the detector orientation. The direction of the incident X-ray beam is opposite to the z axis. The rotation center is the nominal position of the direct beam on the detector head (or in the recorded scattering pattern).

$$\mathbf{R}(\tau, y) = \begin{pmatrix} \cos\tau & 0 & \sin\tau \\ 0 & 1 & 0 \\ -\sin\tau & 0 & \cos\tau \end{pmatrix}. \quad (4)$$

Conversely,

$$\begin{pmatrix} x_0 \\ y_0 \\ 0 \end{pmatrix} = \mathbf{R}^T \begin{pmatrix} x \\ y \\ z+d \end{pmatrix} = \begin{pmatrix} R_{11} & R_{21} & R_{31} \\ R_{12} & R_{22} & R_{32} \\ R_{13} & R_{23} & R_{33} \end{pmatrix} \begin{pmatrix} x \\ y \\ z+d \end{pmatrix}. \quad (5)$$

Note that the matrix elements are uniquely determined by the detector orientation and do not need to be recalculated for each pixel or q value. Also note that the same matrix can also be represented by a different set of three rotation angles, for instance, each about the x-, y- and z-axis. But the values of these angles would not be obvious from the experimental set-up.

Once the physical position of the pixel is known, the scattering angle θ and the azimuthal angle φ can be calculated,

$$\theta = \frac{1}{2}\arcsin|-\hat{\mathbf{r}}\times\hat{\mathbf{z}}| = \frac{1}{2}\arcsin\frac{(x^2+y^2)^{1/2}}{(x^2+y^2+z^2)^{1/2}}, \quad (6)$$

where $\hat{\mathbf{r}} = \mathbf{r}/|\mathbf{r}|$ is the unit vector along the direction of the scattered X-ray, and

$$\varphi = \arctan(y/x). \quad (7)$$

In grazing-incident geometry, the q vector for each pixel must be further decomposed into components along the sample normal (q_n) and within the sample plane (q_r). The components of the scattering vector using laboratory coordinates are

$$\begin{aligned} q_x &= q\cos\theta\cos\varphi, \\ q_y &= q\cos\theta\sin\varphi, \\ q_z &= q\sin\theta. \end{aligned} \quad (8)$$

The components of the scattering vector as observed by the sample that is positioned at the X-ray incident angle of α (sample normal along the y-axis when $\alpha = 0$) are therefore

$$\begin{aligned} q_n &= q_y\cos\alpha + q_z\sin\alpha, \\ q_r &= \left(q^2 - q_n^2\right)^{1/2}. \end{aligned} \quad (9)$$

To perform the inverse translation from (q_r, q_n) to the pixel position (x_0, y_0), the scattering angle θ is first determined from the magnitude of the scattering vector,

$$q = \left(q_r^2 + q_n^2\right)^{1/2}, \quad (10)$$

$$\theta = \arcsin(\lambda q/4\pi). \quad (11)$$

The scattering vector is then projected onto the laboratory coordinate system,

$$q_z = q\sin\theta, \quad (12)$$

$$q_y = \left(q_n - q_z\sin\alpha\right)/\cos\alpha, \quad (13)$$

$$q_x = \left(q^2 - q_y^2 - q_z^2\right)^{1/2}, \quad (14)$$

where q_x takes the same sign as q_r. The corresponding azimuthal angle is therefore

$$\varphi = \arctan(q_y/q_x). \quad (15)$$

The detector pixel corresponding to (q_r, q_n) is located at the intersection of the plane of the detector, *i.e.* $z_0 = 0$, or

$$R_{13}x + R_{23}y + R_{33}(z+d) = 0, \quad (16)$$

and the trajectory of the scattered X-ray

$$\begin{aligned} x &= t\sin2\theta\cos\varphi, \\ y &= t\sin2\theta\sin\varphi, \\ z &= -t\cos2\theta. \end{aligned} \quad (17)$$

Solving equations (16) and (17) gives the position of the pixel in laboratory coordinates,

$$\begin{aligned} x &= \frac{-R_{33}\tan2\theta\cos\varphi}{(R_{13}\cos\varphi + R_{23}\sin\varphi)\tan2\theta - R_{33}}d, \\ y &= \frac{-R_{33}\tan2\theta\sin\varphi}{(R_{13}\cos\varphi + R_{23}\sin\varphi)\tan2\theta - R_{33}}d, \\ z &= \frac{(R_{13}\cos\varphi + R_{23}\sin\varphi)\tan2\theta}{(R_{13}\cos\varphi + R_{23}\sin\varphi)\tan2\theta - R_{33}}d - d. \end{aligned} \quad (18)$$

APPENDIX *B*
Calibration of scattering parameters

In order to utilize the conversions described above, it is necessary to first determine the geometric parameters that define these conversions, namely the sample-to-detector distance d, the beam position in the scattering pattern based on which (x_0, y_0) is determined, and the angles ψ and τ (χ only affects the conversion for grazing-incident scattering data and usually takes the default value of 0). At beamline X9, this calibration is performed by matching experimental scattering patterns from standard powder samples with predicted locations of the corresponding powder diffraction rings.

The pixels on each powder ring are located on a cone defined by the scattering angle. When the surface of the WAXS detector is not perpendicular to the incident X-rays, each ring becomes an ellipse in the scattering pattern (Urban *et al.*, 2003).

For WAXS geometry calibration, multiple standards that produce powder rings spanning the full q-range may be used to increase the accuracy of the calibration. An example is shown in Fig. 6. Automatic refinement of the parameters is possible but currently not implemented in the software used at X9. In this example there are minor discrepancies between the calculated and actual patterns. This can be attributed to the inadequate distortion correction in the software provided by the detector vendor, as has been confirmed by a calibration

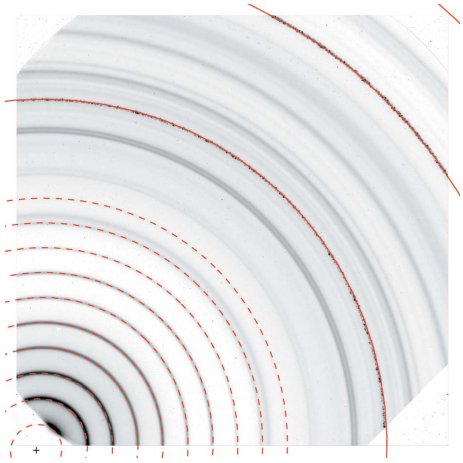

Figure 6
X-ray diffraction patterns and the expected powder diffraction rings from silver behenate (dashed red) and lanthanum boride (solid red) standard samples. The beam center is shown as '+'. The diffraction patterns from the two samples were added together using software.

image recording the positions of X-rays passing through small apertures precisely arranged on a grid of known geometry. Further spatial distortion correction based on the calibration image is possible (Gruner *et al.*, 2002) but has not been implemented since the slight distortion does not affect most of the measurements conducted at X9.

The X-ray energy can be calibrated using the WAXS detector as a fluorescence detector, as discussed in §4.1.

APPENDIX *C*
Analytic form of the polarization and solid angle correction factors

The polarization (*e.g.* Yang & Huang, 2003) and solid angle (Barna *et al.*, 1999) correction factors, $F_{\rm pol}$ and $F_{\rm s.a.}$, can be expressed in terms of the pixel position and the geometric parameters discussed above,

$$F_{\rm pol} = \sin^2\Psi = |\hat{\mathbf{r}}\times\hat{\mathbf{x}}|^2 = \frac{y^2+z^2}{x^2+y^2+z^2}, \qquad (19)$$

$$F_{\rm s.a.} = \cos^3\Theta = |\hat{\mathbf{r}}\cdot\hat{\mathbf{z}}_0|^3 = \frac{|R_{13}x+R_{23}y+R_{33}z|^3}{[x^2+y^2+d^2]^{3/2}}. \qquad (20)$$

Here, Ψ is the angle between the polarization vector of the incident X-rays (assumed to be along the x-axis) and the direction of the scattered X-ray, $\hat{\mathbf{r}}$; θ is the angle between $\hat{\mathbf{r}}$ and the surface normal of the detector, given by

$$\hat{\mathbf{z}}_0 = \mathbf{R}\begin{pmatrix}0\\0\\1\end{pmatrix} = \begin{pmatrix}R_{13}\\R_{23}\\R_{33}\end{pmatrix}. \qquad (21)$$

The measured intensity I and the corrected intensity I_0 are related by

$$I = I_0\, F_{\rm pol}\, F_{\rm s.a.}. \qquad (22)$$

The corresponding pixel position (x_0, y_0) can then be found accordingly using equation (5).

The author thanks Dr Marc Allaire and Professor Hoichang Yang for providing the example data included in this manuscript. The construction of the X9 beamline was a joint effort by the NSLS and the CFN at BNL, with the CFN funding the equipment in the experimental station. The operations of NSLS and CFN are both supported by US Department of Energy, Office of Basic Energy Sciences, under contract No. DE-AC02-98CH10886.

References

Allaire, M. & Yang, L. (2011). *J. Synchrotron Rad.* **18**, 41–44.
Barna, S. L., Tate, M. W., Gruner, S. M. & Eikenberry, E. F. (1999). *Rev. Sci. Instrum.* **70**, 2927–2934.
Bras, W., Dolbnya, I. P., Detollenaere, D., van Tol, R., Malfois, M., Greaves, G. N., Ryan, A. J. & Heeley, E. (2003). *J. Appl. Cryst.* **36**, 791–794.
Chapman, H. N. *et al.* (2011). *Nature (London)*, **470**, 73–77.
Gruner, S. M., Tate, M. W. & Eikenberry, E. F. (2002). *Rev. Sci. Instrum.* **73**, 2815.
Hlaing, H., Lu, X., Hofmann, T., Yager, K. G., Black, C. T. & Ocko, B. M. (2011). *ACS Nano*, **5**, 7532–7538.
Jeng, U.-S., Su, C. H., Su, C.-J., Liao, K.-F., Chuang, W.-T., Lai, Y.-H., Chang, J.-W., Chen, Y.-J., Huang, Y.-S., Lee, M.-T., Yu, K.-L., Lin, J.-M., Liu, D.-G., Chang, C.-F., Liu, C.-Y., Chang, C.-H. & Liang, K. S. (2010). *J. Appl. Cryst.* **43**, 110–121.
Kim, S. H., Jang, M., Yang, H., Anthony, J. E. & Park, C. E. (2011). *Adv. Funct. Mater.* **21**, 2198–2207.
Makowski, L. (2010). *J. Struct. Funct. Genomics*, **11**, 9–19.
Pokric, B., Allinson, N. M., Ryan, A. J., Fairclough, P., Dobson, B. R., Derbyshire, G. E., Helsby, W., Long, G. & Moon, K. (2002). *Nucl. Instrum. Methods Phys. Res. A*, **477**, 329–334.
Rueda, D. R., Garcia-Gutierrez, M. C., Nogales, A., Capitan, M. J., Ezquerra, T. A., Labrador, A., Fraga, E., Beltran, D., Juanhuix, J., Herranz, J. F. & Bordas, J. (2006). *Rev. Sci. Instrum.* **77**, 033904.
Svergun, D. I., Petoukhov, M. V. & Koch, M. H. (2001). *Biophys. J.* **80**, 2946–2953.
Urban, V., Panine, P., Ponchut, C., Boesecke, P. & Narayanan, T. (2003). *J. Appl. Cryst.* **36**, 809–811.
Weigand, S., Stillwell, B., Guise, W., Quintana, J. & Keane, D. (2009). *Adv. X-ray Anal.* **52**, 58–68.
Yang, L. (2005). *Macromol. Res.* **13**, 538–541.
Yang, L. & Huang, H. W. (2003). *Biophys. J.* **84**, 1808–1817.
Yang, L. & Yang, H. (2009). *J. Synchrotron Rad.* **16**, 788–795.